ADVANCED FUNCTIONAL MATERIALS
www.afm-journal.de

Electronic Transport and Interaction of Lattice Dynamics in Topological Nodalline Semimetal $HfAs_2$ Single Crystals

Zahir Muhammad, Ghulam Hussain, Rajbul Islam, Natalia Zawadzka, Md Shafayat Hossain, Obaid Iqbal, Adam Babiński, Maciej R. Molas, Fei Xue, Yue Zhang, M. Zahid Hasan, and Weisheng Zhao**

Topological semimetals represent a novel class of quantum materials displaying non-trivial topological states that host Dirac/Weyl fermions. The intersection of Dirac/Weyl points gives rise to essential properties in a wide range of innovative transport phenomena, including extreme magnetoresistance, high mobilities, weak antilocalization, electron hydrodynamics, and various electro-optical phenomena. In this study, the electronic, transport, phonon scattering, and interrelationships are explored in single crystals of the topological semimetal $HfAs_2$. It reveals a weak antilocalization effect at low temperatures with high carrier density, which is attributed to perfectly compensated topological bulk and surface states. The angle-resolved photoemission spectroscopy (ARPES) results show anisotropic Fermi surfaces and surface states indicative of the topological semimetal, further confirmed by first-principle density functional theory (DFT) calculations. Moreover, the lattice dynamics in $HfAs_2$ are investigated both with the Raman scattering and density functional theory. The phonon dispersion, density of states, lattice thermal conductivity, and the phonon lifetimes are computed to support the experimental findings. The softening of phonons, the broadening of Raman modes, and the reduction of phonon lifetimes with temperature suggest the enhancement of phonon anharmonicity in this new topological material, which is crucial for boosting the thermoelectric performance of topological semimetals.

1. Introduction

Topological materials exhibit distinctive transport properties, including significant magnetoresistance and high carrier mobilities.[1–4] Investigating these phenomena through electronic and structural studies has become a focal point in modern condensed matter physics. The unique nature of these materials was early recognized in band theory,[5] underscoring the fundamental significance of their distinctive bands. In recent years, several remarkable phenomena have been unveiled, such as unconventional surface states,[6] intrinsic anomalous Hall effects,[7] quantum anomalies,[8] extremely large magnetoresistance (XMR),[1–4,9] and weak antilocalization.[10] Significantly, condensed quantum matter has witnessed cutting-edge research with the revelation of topological Dirac states and the emergence of Weyl semimetals.[11–13]

The emerging class of topological materials, specifically early transition metal mono/dipnictides MX/MX_2 (M = Mo, W, Ta, Nb, Hf, Zr; X = Te, P, As, Sb), has

Z. Muhammad, Y. Zhang, W. Zhao
Hefei Innovation Research Institute
School of Integrated Circuit Science and Engineering
Beihang University
Hefei, Anhui 230012, P. R. China
E-mail: yz@buaa.edu.cn; weisheng.zhao@buaa.edu.cn

G. Hussain
Institute for Advanced Study
Shenzhen University
Shenzhen 518060, P. R. China

R. Islam, F. Xue
Department of Physics
University of Alabama at Birmingham
Birmingham, AL 35294, USA

N. Zawadzka, A. Babiński, M. R. Molas
Institute of Experimental Physics
Faculty of Physics
University of Warsaw
Pasteura 5, Warsaw 02-093, Poland

M. S. Hossain, M. Z. Hasan
Laboratory for Topological Quantum Matter and Advanced Spectroscopy (B7)
Department of Physics
Princeton University
Princeton 08540, NJ, USA

O. Iqbal
Institute of Solid-State Physics
Chinese Academy of Sciences
Hefei, Anhui 230031, P. R. China

The ORCID identification number(s) for the author(s) of this article can be found under https://doi.org/10.1002/adfm.202316775

DOI: 10.1002/adfm.202316775

undergone extensive study in recent years, particularly as Weyl semimetals.[1–4,9–19] Early transition metal dipnictides (TMDPs) are primarily characterized by non-trivial topological properties, offering exciting features with potential future applications. TMDPs have demonstrated contributions to superconductivity,[20,21] significant thermoelectric responses,[22,23] and photodetection,[24] all stemming from their non-trivial band topology.

Transport and ARPES, coupled with theoretical studies, have been employed in recent years to investigate the topological states in TMDPs, including MAs_2 and MP_2 (M = Mo, W, Ta, Nb, Hf, Zr).[2,13,16,17,19,25–27] Notably, the topological surface states and nodal loop Fermi surface have been observed in HfP_2 and ZrP_2.[17,18] An XMR was predicted in ZrP_2, attributed to electron-hole compensation and topological surface states.[19] X. Zhou et al. predicted butterfly-shaped nodal lines in $ZrAs_2$,[18] opening a new avenue for exploring topological properties in group IV TMDPs.

Electron-phonon scattering in these kinds of materials involves interactions between interband electrons and phonons across different energy bands. The electron scatters with a phonon from a distinct energy band, changing momentum and energy levels. The electron scatters with a phonon from a distinct energy band, resulting in changes in energy and momentum. The electron-phonon coupling significantly influences the electrical conductivity by changing the carrier mobility and density in the electrical transport of topological semimetals.[28–30] Previous investigations have suggested that electron-phonon coupling and electron-electron coupling influence macroscopic transport properties.[31] In a related study, Jin et al. explored electron-phonon coupling alongside phonon–phonon coupling in large magnetoresistance topological semimetals $TaAs_2$ and $NbAs_2$,[32] indicating the critical role of these interactions in the transport properties of such materials. The scattering of electrons holds significance in assessing the lattice's influence on transport and heat properties. The scattering of electrons via phonons can affect charge carriers, leading to improved conductance.[32,33] The pronounced phonon-electron coupling in topological semimetals (TSM) has been predominantly reported through optical spectroscopy techniques, which can directly probe the system's phonons.[34–36]

Phonon scattering further plays a pivotal role in understanding thermoelectric materials by studying lattice thermal conductivity and phonon anharmonicity, as essential for comprehending thermoelectric performance in thermionics. The variation of phonon energies results in distinct velocities and, consequently, different scattering ratios, leading to varying thermal conductivity.[37,38] Although acoustic phonon branches traditionally receive emphasis in heat conduction because of their high velocities. Recently, optical branches have gained reconsideration owing to their higher energy and short mean free path, sometimes proving more crucial by influencing the band structure. In materials like PbSe (PbTe), ≈25% (22%) of thermal conductivity (κ) is derived from optical branches.[39] Additionally, low-energy optical phonons offer scattering channels for acoustic phonons.[40] For heat conduction, phononic dispersions, density of states, and anharmonicity interplay of phonon branches are indispensable. Several theoretical studies have reported such findings, which are consistent with the results obtained from other techniques.[41–44] However, there is limited research on the phonon–phonon or phonon-electron interactions and the dynamic properties of the lattice in these systems. Recent reports on the topological properties of HfP_2[17] and ZrP_2,[19] particularly ZrP_2 exhibiting XMR, have generated increased interest. Therefore, we conducted a more in-depth exploration by growing single crystals of $HfAs_2$ and investigating their structural, transport, electronic, and phononic properties.

We have grown the $HfAs_2$ single crystals, classified under the $OsGe_2$ group, with a $PbCl_2$-type orthorhombic structure in space group *C1/m* (No. 12), and SG *Pnma* (No. 62).[45] We have studied the electronic properties of the grown crystals using high-resolution ARPES) and transport measurements and further confirmed them by first-principle DFT calculations. We conducted angular and temperature-dependent Raman experiments on the single crystal $HfAs_2$ for the lattice dynamics of this new compound. To complement our experimental findings, we employed phonopy, phono3py, and VASP packages to compute phononic dispersion, density of states, lattice thermal conductivity, and phonon lifetimes.

2. Results and Discussion

Single crystals of $HfAs_2$ were grown using the chemical vapor transport (CVT) method. Raw material powders with a stoichiometric ratio of Hafnium (Hf) (purity of 99.95%) and Arsenic (As) foil (purity of 99.99%) were mixed in a 1:2 ratio and sealed in a quartz tube under a vacuum pressure of 5×10^{-4} Torr. These quartz tubes were placed in a commercial CVT furnace, and the temperature was set to 850 °C at a rate of 50 °C h^{-1}, where they were kept for four days. During this period, Hafnium reacted completely with arsenic, forming polycrystalline $HfAs_2$. The resulting polycrystalline material was ground into powder and iodine was introduced as a transport agent. The mixture was then sealed in the same manner and placed back into the CVT furnace. The ampule was heated to a temperature gradient of 850 and 750 °C at a rate of 100 °C h^{-1} and maintained at this gradient for two weeks before being gradually cooled down to room temperature at 50 °C h^{-1}. The completion of the experiment yielded 3D polyhedral-like single crystals, as depicted in the inset in **Figure 1b**.

The orientation plane of the single crystals and their crystallographic structure were determined through powder X-ray diffraction (XRD). $HfAs_2$ belongs to the Pnma (No. 62) space group, as illustrated in Figure 1a. Its crystal structure exhibits an orthorhombic configuration akin to the $PbCl_2$-type. Figure 1b displays the X-ray diffraction pattern of the as-grown $HfAs_2$ alongside its Rietveld analysis. Compared with calculated patterns, the Rietveld analysis of the XRD data confirms a precise match with the $HfAs_2$ phase (DB Card No: 42 916, ICDD (61 0636)). This analysis reveals that $HfAs_2$ possesses an orthorhombic crystal structure, with the extracted lattice parameters measured as a = 6.768(10) Å, b = 3.672(5) Å, and c = 8.934(13) Å.[45] The structure of $HfAs_2$ is formed in three-dimension, the 4- Hf^{4+} ions are bonded with 8-As^{2-} ions, with the crystal orientation perpendicular to the (00X) plane. The single-crystal XRD (see Figure S1, Supporting Information) can show the sharp peaks of the (00X) plane. The inset in Figure 1b displays an optical image of the grown crystals with sizes ranging from ≈1 to 3 mm in length, exhibiting a polyhedral shape. The stoichiometric ratio of the grown

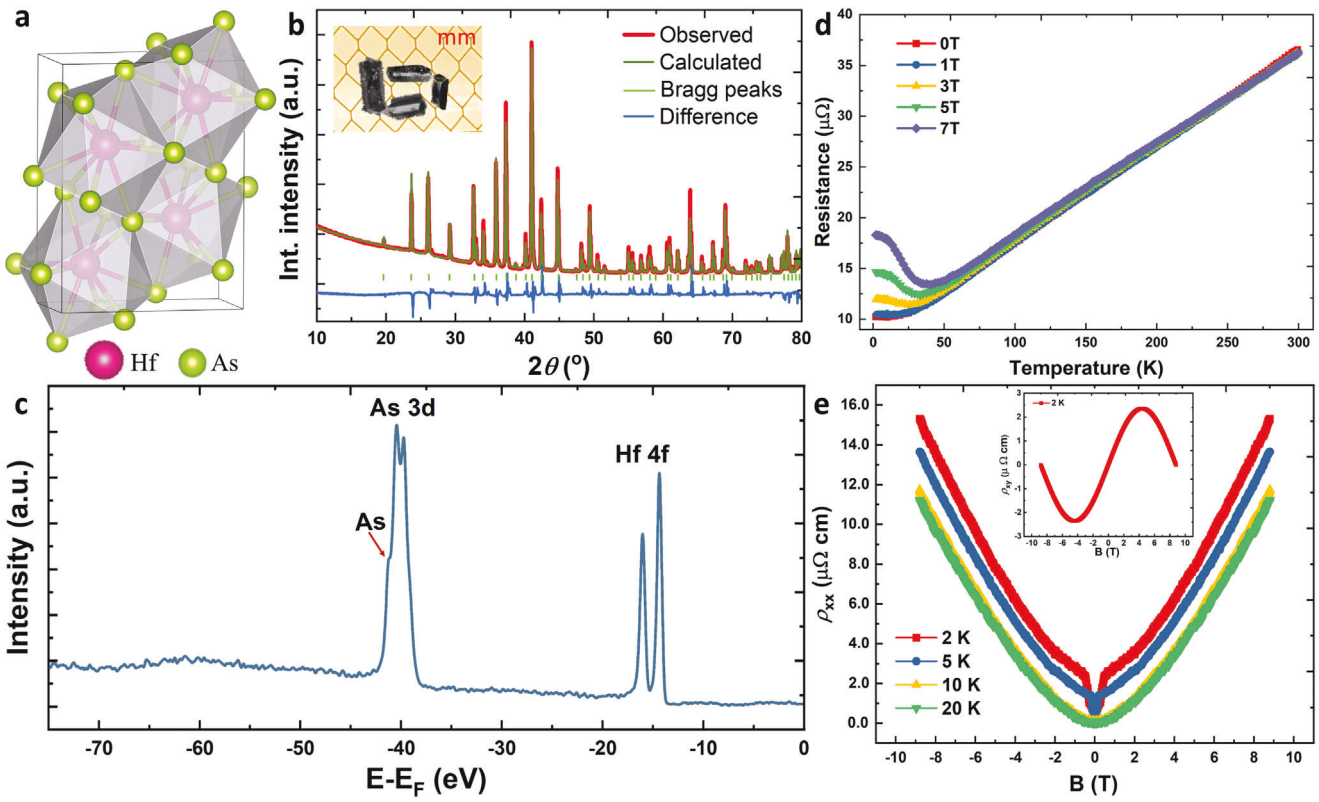

Figure 1. a) Crystal structure of $HfAs_2$ shows $PbCl_2$-type orthorhombic structure. b) XRD patterns of $HfAs_2$ and their Rietveld analysis, inset: the image of the single crystals. c) Core-level photoemission spectra of $HfAs_2$ and measured with 120 eV photon energy. d) Resistance versus temperature dependence curves at various magnetic fields from 0 to 7 T and e) longitudinal resistivity (ρ_{xx}) as a function of perpendicular magnetic field (B) at $T = 2$, 5, 10, and 20 K, and inset: transverse resistivity (ρ_{xy}) at 2 K of $HfAs_2$, respectively.

crystals was confirmed by energy-dispersive X-ray spectroscopy (EDS) (see Figure S2a, Supporting Information), showing an elemental composition of Hf and As at ≈1:2. Figure S2b–d (Supporting Information) presents elemental mapping, demonstrating the homogeneous distribution of Hf and As in the bulk crystals. Figure 1c presents the integrated core-level photoemission spectrum of the single crystal, revealing Hf *4f* and As *3d* spin-orbit doublets that can further verify the chemical composition of the $HfAs_2$ crystal. The doublet peak between 14 and 17 eV is assigned to a replica Hf *4f* state originating from the Hf surface's chemical shift, while the peak within 40 to 42 eV is attributed to the As *3d* state from the As surface. We also observed the shoulder peak in the As peak of $HfAs_2$, which can probably reveal the excess As.

A four-electrode device was fabricated on an $HfAs_2$ crystal to investigate its transport properties, as depicted in Figure 1d,e. Figure 1d displays the longitudinal resistance as a function of temperature under various magnetic fields. At $B = 0$ T, the resistance gradually decreases as the temperature decreases from 300 K to ≈2 K (Figure 1d), resulting in a residual resistance ratio (R_{300K}/R_{2K}) (RRR) for $HfAs_2$ of ≈3.562. The lower residual resistance ratio indicates a rapid decline in resistance upon reaching 2 K. The lower RRR of $HfAs_2$ can be attributed to a larger disorder compared to other TSM.[2,19,26,46] The resistance above 50 K appears relatively unchanged with a magnetic field. However, below 30 K, the resistance shows a strong dependence when the magnetic field (B) becomes ≥3 T. Below 35 K, a noticeable upturn is observed ≈35 K as the field increases to 3 T, and a plateau-like saturation emerges below $T = 30$ K in R (B, T), as illustrated in Figure 1d. The resistance doubles as B increases to 7 T at low temperatures, and this effect is expected to be further enhanced with a higher B. These results indicate a magnetic field-induced transition from a metallic profile (at high temperatures) to a semiconducting profile (at low temperatures). A similar field-induced transition-like behavior has been reported in other types of topological and semimetals[2,3,9,46–49] due to multiple types of carriers. However, at high temperatures, $HfAs_2$ exhibits metallic behavior with a positive temperature coefficient of resistance (dR/dT > 0), even under high magnetic fields. This observation implies that phonon scattering may dominate the transport behavior.[50]

In Figure 1e, the longitudinal resistivity is presented as a function of magnetic field (B) at various low temperatures. The resistivity demonstrates an increasing trend with the elevation of the magnetic field for all tested temperatures. We have calculated the magnetoresistance (MR) value for the sample is approximately 4034% at $B = 9$ T and 2 K. Interestingly we have observed the sharp cusps in ρ_{xx} below 10 K [refer to Figure 1e; Figure S3a, Supporting Information], however, these cusps tend to disappear as the temperature increases above 5 K, transforming into a parabolic shape of linear magnetoresistance (LMR). The cusp in our sample is attributed to the quantum interference phenomenon, such as the weak antilocalization (WAL)

effect, which was previously observed in other topological, Weyl, and nodal line semimetals.[51–54]

The cusp at 2 K displays two plateaus with a very sharp and deep, indicating the pronounced emergence of a strong WAL effect. The WAL effect in $HfAs_2$ is attributed to the intricate interplay between spin-orbit coupling and larger disorder (can be seen from the core level spectra and its lower RRR). Additionally, we have determined the carrier density of electrons (e) and holes (h) at 2 K (see the inset in Figure 1e) from the transverse resistivity (ρ_{xy}) versus the magnetic field (B). The ρ_{xy} versus B data further reveals that as the temperatures increase, the ρ_{xy} curves transition to a linear behavior (see Figure S3b, Supporting Information). We further analyze that for the Hall conductivity,$\sigma_{xy} = \rho_{xy}/(\rho^2_{xy} + \rho^2_{xx})$ and fitted with a two-band model of carriers (see Figure S2c, Supporting Information) to estimate the carrier density and carrier mobility at 2 K.[54]

$$\sigma_{xy} = \left[\frac{n_e\mu_e^2}{1+\mu_e^2B^2} + \frac{n_h\mu_h^2}{1+\mu_h^2B^2}\right] eB \quad (1)$$

Here, $n_{e,h}$ represent the carrier density of the electron and hole and $\mu_{e,h}$ denote the carrier mobility of electrons and holes, respectively. Due to plateaus at low magnetic, the data shows a nonlinearity in the σ_{xy} data (see Figure S3c, in Supporting Information). The estimated n_e is 3.35×10^{21} μΩ cm^{-3}, n_h is 2.91×10^{20} μΩ cm^{-3}, and μ_e is $\approx 1.04 \times 10^3$ cm^2 $V^{-1}S^{-1}$, and μ_h is $\approx 1.46 \times 10^3$ cm^2 $V^{-1}S^{-1}$, respectively for 2 K. The carrier density and mobility can be further changes with temperature variation. The estimated carrier densities are comparable to other topological and weyl semimetals.[19,20,25,54] The discrepancy between n_e and n_h indicates that $HfAs_2$ is not perfectly compensated semimetal, which can be affected by compensation from the trivial nodal loop and open-orbit topological material.[51,52]

To investigate the electronic structure of these newly grown TMDP $HfAs_2$ single crystals, we performed high-resolution ARPES combined with first-principles calculations, as shown in **Figure 2**. The electronic band structure and Fermi surface were directly observed from ARPES and first-principles calculations. Figure 2a indicates the 3D Brillouin zone (BZ) with high-symmetry momentum points marked by blue lines. Figure 2b,c represents the calculated 3D bulk Fermi surfaces (FSs) from DFT calculations. The calculated FS show the electrons and hole-like pockets, which are further compared with the constant-energy contour (CEC) plots in the first BZ (see Figure 2d) along the high-symmetry direction. The CEC shows that the Fermi surface has three Fermi sheets that consist of four electron-like pockets on the Fermi surface sheets around Γ (see Figure 2d), each apex pointing toward the X point. The CEC at 44 eV was cut at different binding energies from 0 to −0.5 eV (see Figure S4a, Supporting Information). With decreasing energy levels from the Fermi level, the bulk states merely enlarge, and the small pockets at the X point become bigger and make a clear rectangular shape stripelike FS from the boundaries.

We further calculated the electronic bulk band structure in Figure 2e using all the k-points in the first BZ. The calculated band structure shows both the electron- and hole-like bands crossing near the Fermi level, which indicates the metallic behavior of the sample. The bands crossing along Γ-X and around Y-Γ-Z points indicate the nodal line semimetal with multiple nodal loops. We also observed open-ended and extended indefinitely bands at some high-symmetry lines in the BZ. The band structure was further studied through ARPES along the high symmetry path Γ-X at 42 eV (see Figure 2f). The highlighted band indicates a close comparison with the calculated bulk band structure in the acquired direction. The band dispersion revealed that the conduction band region near the point shows parabolic hole-like bands, which nearly crossed the Fermi level. Due to 3D needle type shape materials, it shows different termination of the cleavage surface, which can be seen that the Γ-X is not clearly observed in the BZ. Therefore, we see half of the band and other bands are observed from another termination as well. At the same time, we calculated the surface bands and the Fermi arc along the (001) surface and compared them with ARPES results. Figure 2g reveals the calculated Fermi surface along (001) projected surface. The distribution of these nodal loop line Fermi arc can be seen at $k_x = 0$. While the loops are extended in large k_x. Whereas, Figure 2h indicates the CEC plot measured at 36 eV. At Γ point, we can clearly see the pocket indicating the surface states, which was absent at 42 eV photon. The FS indicates that the sample shows a rectangular shape around the Γ point in Γ-X direction. In extended BZ we can see the clear nodal loop. The CEC at different binding energies revealed that in the lower binding energies, the rectangular shape stripelike FSs are more clear (see Figure S4b, Supporting Information). The parabolic-like Fermi pockets at the X-point show the surface states surrounding the bulk pocket away from the Fermi level below 400 meV. The calculation and experimental results show the anisotropic FS of $HfAs_2$. Surface calculations revealed that the $HfAs_2$ shows the surface states on the (001) project surface (see Figure 2i). However, the dispersion of the energy-momentum cut along the Γ-X in our experiments further illustrates these surface states as shown in Figure 2k, measured at 36 eV photonenergy with clear electrons and hole like bands are matched well with the surface calculations, which was absent in 4 eV. While, due to different surface terminations, the bulk states dominate the cut with some extend, so it is hard to distinguish the nontrivial surface states in these results and to compare them with the theoretical calculations properly for some high directions. However, along the X-direction, they are in good agreement with each other. We can also see the Dirac-like states in the lower binding energy along the X direction in both the experimental and theoretical results. The observed nodal lines (see Figure 2i,k) in our sample, can often exhibit unusual magnetoresistance properties due to the unique band structure. Moreover, we have performed the photon energy-dependent ARPES measurements to evaluate k_z dispersion (see Figure S5, Supporting Information). The band dispersion shows that the position dispersion maps change with photon energy. The linear dispersion distinct from the Fermi level looks to be strongly photon energy dependent. With increasing photon energy the bulk states begin to merge with the surface instead. This is an indication of the non-trivial topological surface states. Therefore, our results show that $HfAs_2$ is a topological nodal semimetal. We also analyzed the energy distribution curves (EDC) and the momentum distribution curves (MDC), which also show the different positions of the energy and momentum space (see Figure S6, Supporting Information). The spectral weight can distinguish the different

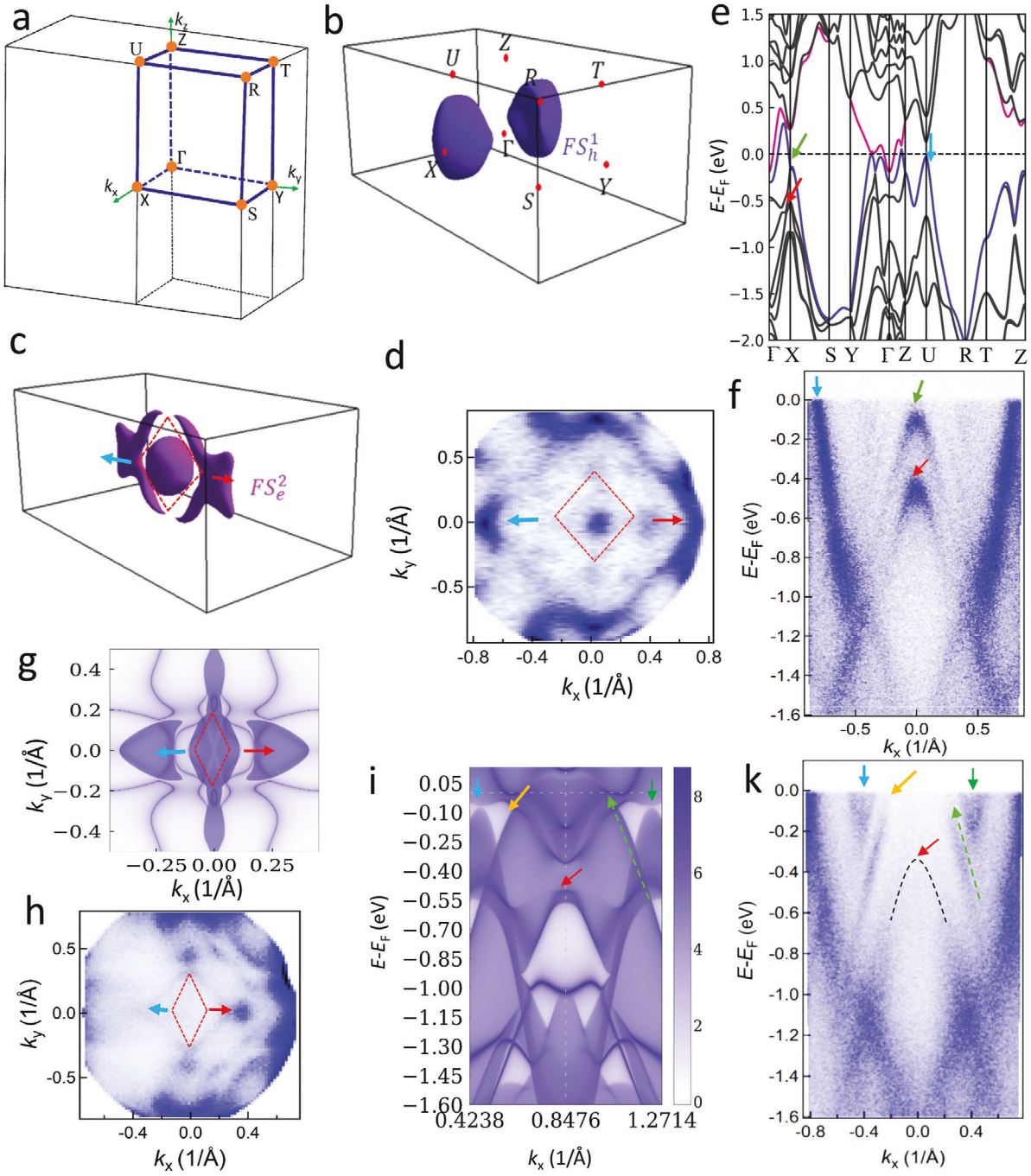

Figure 2. First-principles calculations and ARPES of $HfAs_2$. a) The first BZ of the PbCl2-type orthorhombic structure, b,c) calculated 3D Fermi surfaces and d) the measured CEC plot $HfAs_2$ at 42 eV. e) The calculated bulk band structure of $HfAs_2$ for the whole BZ and f) the measured band dispersion cut along the high symmetry Γ-X direction represents the bulk-like bands measured at 42 eV using ARPES, and the marked arrows represent the comparison with the calculated bands. g) The calculated Fermi surface projected on (001) surface and h) CEC map measured at 36 eV for $HfAs_2$, i,j) calculated surface band projected on (001) plane and the measured energy-momentum cut along the high symmetry Γ-X direction from ARPES at 36 eV for $HfAs_2$, respectively. ARPES experiments were performed at 14 K.

energy distributions near the Fermi level in the EDC spectra, which identify the photon energy dependence.

Moreover, it is uncertain which factors contribute to this transport behaviour of TMDPs. It is obvious that better carrier mobility can be attributed to topologically protected surface bands. However, the origin of the weak antilocalization effect and other transport properties in $HfAs_2$ can be induced by a larger disorder and strong spin-orbit coupling, as well as maybe a certain role of electron/phonon scattering in this new TMS.

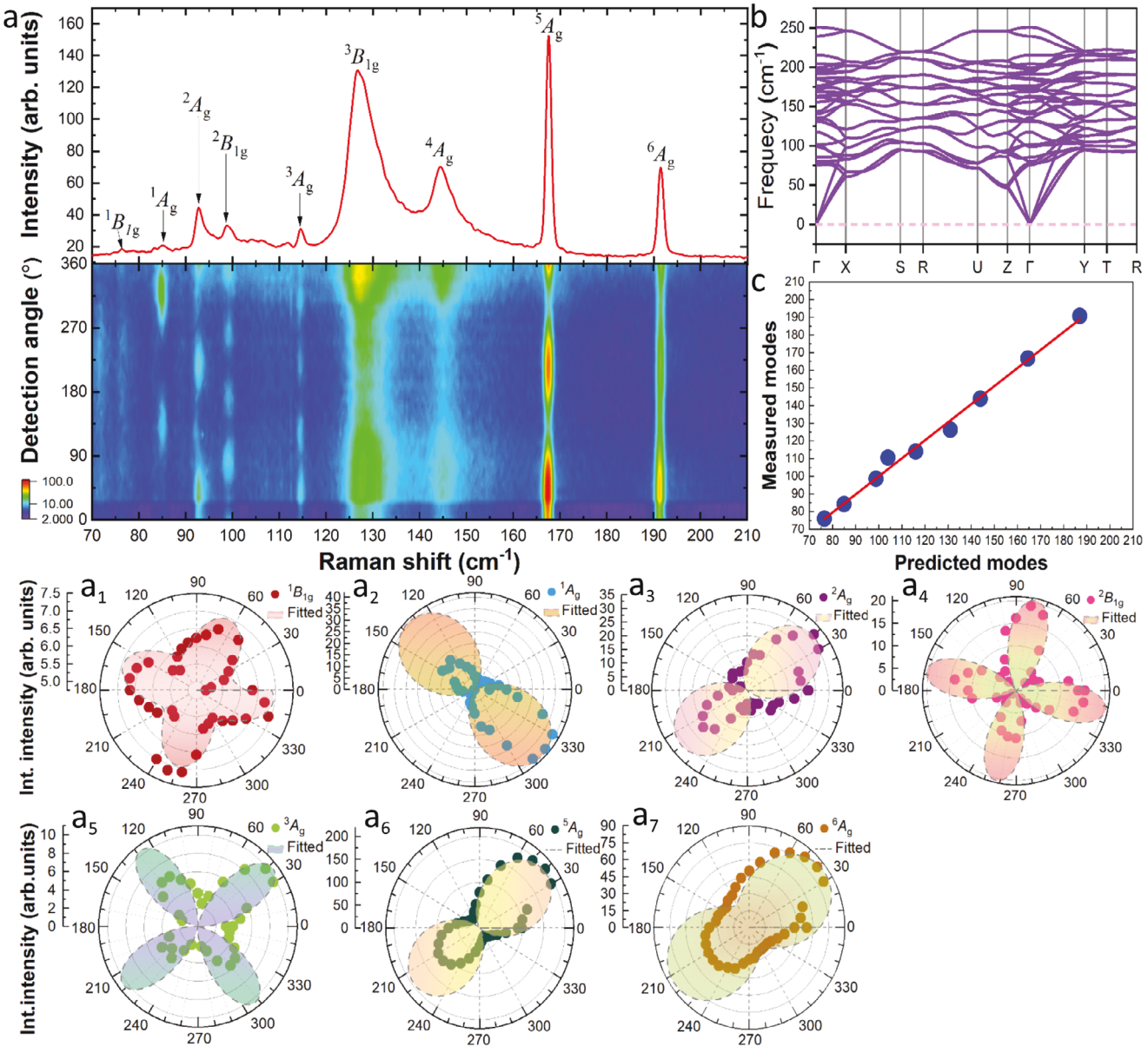

Figure 3. a) Raman spectrum (upper pennel) measured at 5 K and contour map (down pennel) of polarization spectra at different detection angles from 0–360^0 under the co-(XX) linear configuration. a_1–a_7) Polar plots of the Raman modes (^1A_g, $^1B_{1g}$, ^2A_g, ^3A_g, $1B_{1g}$, ^5A_g, and ^6A_g) with integrated intensities and their fitting, respectively. b) Phonon band structure of $HfAs_2$. c) Experimentally measured modes versus the predicted modes in cm^{-1}. The solid red line illustrates the ideal agreement.

To further investigate this, we conducted detailed Raman spectroscopy and theoretical investigations for structural lattice dynamics. We performed polarized Raman experiments on as-grown $HfAs_2$ single crystals, leading to the observation of nine Raman active modes, as illustrated in **Figure 3**. Raman spectra were obtained at a temperature of 5 K with measurements taken at various rotational angles, as illustrated in Figure 3. Raman intensities exhibit variations with different incident angles, as depicted in the contour-color map of the polarized Raman spectra taken at varying angles (0°–360°), at co-(XX) linear polarization, as shown in Figure 3a. The contour-color map encodes the intensity evolution as a function of angle, highlighting the polarization effect. The intensity of these Raman spectra depends on both the incident and scattered light, which can be expressed as:

$$I \propto \left|\hat{e}_i \cdot \mathfrak{R} \cdot \hat{e}_s\right|^2 \quad (2)$$

where I is the intensity Raman spectrum, $\hat{e}_i$ and $\hat{e}_s$ are the polarization unit vectors of the incident and scattered light, while $\mathfrak{R}$ denotes the Raman scattering tensor. For the Cartesian coordinate system, $\hat{e}_i$ and $\hat{e}_s$ are fixed in the x–y plane. By the rotational angle of y, $\hat{e}_i = (\cos(\theta + \theta_0), \sin(\theta + \theta_0), 0)$ for the incident light, and $\hat{e}_s = (\cos(\theta + \theta_0), \sin(\theta + \theta_0), 0)$ for the scattered light in the parallel polarization configurations (the polarization angles

of the incident and scattered lights are the same), respectively. The Raman tensors related to each of the irreducible representations of $HfAs_2$ are determined by the 3 × 3 matrix symmetry of phonon mode for backscattering:[55]

$$A_g = \begin{pmatrix} a & 0 & 0 \\ 0 & b & 0 \\ 0 & 0 & c \end{pmatrix}, \quad B_{1g} = \begin{pmatrix} 0 & 0 & e \\ 0 & 0 & 0 \\ e & 0 & 0 \end{pmatrix} \tag{3}$$

The aforementioned Raman tensors point to the symmetry of a given phonon mode. To investigate its angle dependence, the θ angle needs to be included in the analysis, which describes the in-plane spatial dependence of the phonon modes. The θ angle can be considered as the angle between of an arbitrary in-plane axis, for example a or c, and then the incident polarization light. Consequently, the intensities of the A_g and B_{1g} modes will vary differently with the changing θ angle. This means that the observed Raman peaks can be assigned to A_g and B_{1g} modes accordingly through different polarization configurations and symmetry analysis. The intensity variation of different modes is illustrated and plotted in polar plots in Figure 3a$_1$–a$_7$, which can clearly indicate the polarizations of incident and scattered light. While the remaining three peaks do not show a polarization effect (see Figure S7, Supporting Information). Under, $\hat{e}_i \parallel \hat{e}_s$ configuration, the symmetry of three modes ($^1B_{1g}$, $^2B_{1g}$ and ^3A_g) are fourfold and four modes (^1A_g, ^2A_g, ^5A_g, and ^6A_g) are twofold, while two modes ($^3B_{1g}$ and ^4A_g) are unpolarized (see Figure S7, Supporting Information). The gray dotted line shows the fitting using the equations $|a + b\cos^2(\phi)|^2$ and $|e\sin(2\phi)|^2$ for A_g and B_{1g} at co-polarization, respectively. Note that the discrepancy between the experimentally obtained polarization evolutions of the phonon intensities and the fitted curves (see, for example, Figure 2a$_2$) originates from the misalignment of the excitation/detection beam in the experimental setup. However, it does not cover the total symmetry shape of the phonon modes, as it still can be nicely described by the fitting formulas. To summarize, the phonon intensity varies differently at polarization angles, and the modes show different polarization symmetry.

Moreover, ab initio calculations are carried out to study phonon dispersion and predict the modes observed in the Raman spectra. Taking into account the detailed symmetry properties of $HfAs_2$, the phononic band structure shown in Figure 3b exhibits 3 acoustic and 33 optical modes because the primitive cell of $HfAs_2$ contains 12 atoms, with all the atoms occupying the 4c Wyckoff position. The mechanical representation of the modes is estimated as: $M = 6A_{g+} 3A_{u+} 3B_{1g+} 6B_{1u+} 6B_{2g+} 3B_{2u+} 3B_{3g+} 6B_{3u}$. A_g, B_{1g}, B_{2g}, and B_{3g} are the Raman active modes, whereas, the other modes are IR active modes. Further investigation of their nuclear site group supports this finding.[55] It is observed that the vibrational modes at the Brillouin zone center consist of 18 Raman-active modes that can be represented as: $6A_g + 3B_{1g} + 6B_{2g} + 3B_{3g}$ from the symmetry analysis, which is consistent with calculations. The experimentally measured modes versus the predicted modes obtained by DFT are shown in Figure 3c. The solid diagonal line illustrates the ideal agreement between the two approaches. Moreover, the irreducible representation of nine vibrational modes observed in the Raman spectrum is computed by ab initio calculation (see Figure S8, Supporting Information). From the nuclear site symmetry analysis of the space group *Pnma* contains 18 Raman active modes, while the other modes are IR active. However, due to the backscattering arrangement of our experiment, we have only observed the A_g and B_{1g} modes. The modes were further predicted from the DFT calculations and compared with the calculated modes (see Table S1, Supporting Information). It is seen, that the vibrational modes appeared at 143.9, 166.7, and 190.7 cm^{-1} purely originated from the vibrations of As atoms, while the rest of the phonon modes are associated with the vibrations of Hf, and As atoms. All the phonon modes are positive, showing no imaginary frequencies, which reveals that $HfAs_2$ is a dynamically stable material. This is a direct confirmation that our structure is stable at finite temperatures that support the experiments. Also, the phonon dispersion reveals that there are no phonon energy bandgaps in the whole range, which is closely related to the phonon scattering processes. Such a continuous band structure of phonons allows for plenty of scattering paths to the phonon branches. Principally, it is very significant for the low-energy optic and acoustic branches.

To investigate the phonon–phonon and electron-phonon interactions, the Raman scattering of single crystal $HfAs_2$ was further measured as a function of temperature from 5 to 300 K, as shown in **Figure 4a**. With temperature cooling, all the phonon peaks become sharper and shift toward higher frequency as the temperature changes from 300 to 5 K (see Figure 4a). The previously reported results indicated an unusual increase in the linewidth and a decrease in the phonon mode energies, which is interpreted to be evidence of electron-phonon coupling.[42] We further fitted the Raman shift and the linewidth of the observed phonon peaks as a function of temperature to extract the quantitative values via a Voigt function. The line shape of the Raman shift as a function of temperature (see Figure 4a) with the large shift observed in ^4A_g of ≈2% and the lowest shift observed at ≈0.15% in ^2A_g. These results could reveal the possible indication of the phonon anharmoncity or phonon–phonon coupling effect.[56] The signatures of phonon–phonon or electron-phonon couplings in the temperature dependence can be observed from the changes in phonon energy. The phonon energy decreases with increasing temperature due to lattice anharmonicity and/or lattice expansion.[56,57] From the temperature-dependent Raman data shown in Figure 4b, it can be seen that as the temperature increases the Raman modes are shifted to lower energies. The linewidth in Figure 4c indicates the temperature dependence, which is anticipated to anharmonic phonon decay. The temperature-dependent phonon energies and linewidth have contributions from multiple sources, such as lattice thermal expansion and lattice anharmonicity of the phonon interaction. The temperature-dependent phonon energies shift and linewidth can be fitted using the Klemens model;[58]

$$\omega(T) = \omega_0 + A\left[1 + \frac{2}{(e^x - 1)}\right] + B\left[1 + \frac{3}{(e^y - 1)} + \frac{3}{(e^y - 1)^2}\right] \tag{4}$$

and

$$\Gamma(T) = \Gamma_0 + C\left[1 + \frac{2}{(e^x - 1)}\right] + D\left[1 + \frac{3}{(e^y - 1)} + \frac{3}{(e^y - 1)^2}\right] \tag{5}$$

where ω_0 and Γ_0 is the harmonic frequency and linewidth at zero temperature for the optical modes, respectively; $x = \hbar\omega/2k_BT$,

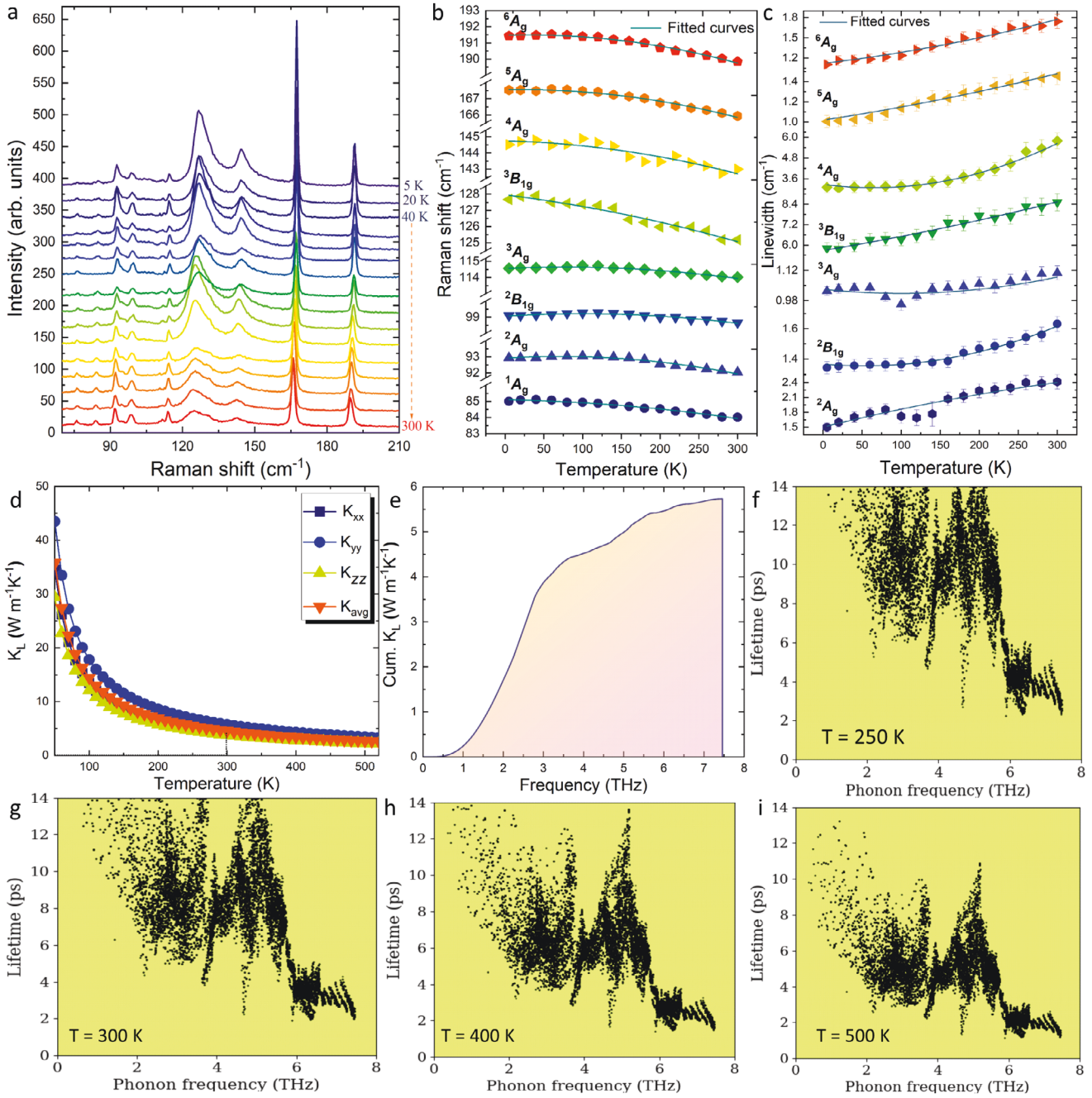

Figure 4. Raman measurements of $HfAs_2$ a) Raman spectra measured at temperatures from 5 K to room temperature, b,c) Raman shift and linewidth of different peaks as a function of temperature and their fitting. The gray line shows the fitting. d) Lattice thermal conductivity is calculated as a function of temperature. e) Cumulative lattice thermal conductivity is computed at room temperature. f–i) phonon lifetimes computed at different temperatures.

$y = \hbar\omega/3k_BT$, while $\hbar$ is the Planck constant, ω is the frequency, k_B is the Boltzmann constant. A, C, B, and D represent the anharmonic constant coefficients related to the three- and four-phonon processes, respectively. The data in Figure 4b,c were fitted using Equations (3) and (4) to extract the fitting parameters, as seen in **Table 1**. The gray line shows the fit of the model, which reproduces our experimental data very well. The linewidth follows the dependence anticipated from the model of anharmonic decay, which is confirmed by the fitting curve. The availability of phonon decay data reveals that phonon–phonon scattering predominantly occurs over electron-phonon scattering for most modes. The linewidths of the two modes, ^2A_g and ^3A_g (see Figure 4c; Figure S9, Supporting Information), exhibit a nonlinear trend with temperature that cannot be fitted using the Klemens model. As temperature increases, the phonon linewidth generally increases; however, within the temperature range of approximately 80 to 140 K, these modes display an anomalous behavior that cannot be well-fitted by the Klemens model.

Table 1. Raman modes fitting and extracted parameters.

Parameters	Raman Modes							
	^1A_g	^2A_g	$^2B_{1g}$	^3A_g	$^3B_{1g}$	^4A_g	^5A_g	^6A_g
ω_o (cm^{-1})	85.1	92.91	99.06	114.56	127.96	144.74	167.55	191.47
A (cm^{-1})	−0.0085	0.0097	0.0031	0.0022	−0.0059	−0.0013	0.0081	0.0014
B (cm^{-1})	−0.0001	−0.0002	−0.0002	−0.0001	−0.0001	−0.0008	−0.0002	−0.0002
Γ_o (cm^{-1})	–	1.50	1.36	1.033	5.62	3.275	1.018	1.122
C(cm^{-1})	–	0.0038	0.0045	0.0037	0.0076	0.0059	0.0012	0.0014
D (cm^{-1})	–	0.0002	0.0004	0.00002	0.00006	0.000046	0.000012	0.000027

However, the other modes are well-fitted with the Klemens model that can confirm that the Raman spectra of $HfAs_2$ show the standard anharmonic phonon–phonon interaction. The anharmonicity is further confirmed by the temperature dependence of the mode energy shifts. It is further suggested that the increasing trend of the phonon linewidth with increasing temperature is associated with the phonon lifetime[59] and the phonon lifetime is directly linked with thermal conductivity. Therefore, we have considered the anharmonic third-order interatomic force constants computation to calculate the lattice thermal conductivity (κ_L) and phonon lifetimes within the single-mode relaxation time approximation approach for $HfAs_2$ to show the thermoelectric response. The temperature-dependent lattice thermal conductivity κ_{avg} together with κ_{xx}, κ_{yy}, and κ_{zz} along the three lattice vectors is depicted in Figure 4d. The room temperature κ_{avg} is indicated by a dotted line with a value of 4.2 $W\,m^{-1}K^{-1}$. The κ_L magnitude along the three directions differs very slightly, given that the low- and high-temperature phases remain structurally similar. The value of κ_L is expected as an upper limit since the relaxation time approximation considers only the scattering through three-phonon processes, whereas it does not include the effects of boundary scattering, structural defects, and the high-order phonon interactions such as electron-phonon scattering.[60] In Figure 4e, we show the cumulative lattice thermal conductivity at room temperature as a function of frequency, revealing that modes from the entire phonon spectrum are not contributing to heat transport. In fact, the optical modes are more responsible compared to the acoustic modes and span over a wide range of frequencies. This trend is different from that of SnSe[61] and other compounds such as GaAs and CdTe,[62] where the acoustic modes are responsible for most of the heat transport. The suppression of heat conduction from the acoustic modes and the substantial role of the optical modes in heat transport are also observed in $MAPbI_3$.[63]

The phonon linewidth is directly related to the phonon lifetimes or the scattering ratios.[64,65] The evolution of the linewidth of different Raman modes as a function of temperature in Figure 4c indicates a reduction of phonon lifetimes with increasing temperature. To support this, we investigated the phonon lifetimes of $HfAs_2$ by calculating the third-order force constants within the single-mode relaxation-time approximation. Figure 4f–i shows the phonon lifetimes as a function of frequency calculated at different temperatures. With increasing temperature, the lifetimes decrease. At 250 K the lifetime is >20 ps, however, at 500 K it becomes <10 ps. These short lifetimes will show the small group velocities with nanometre-scaled mean free paths to be obtained. Furthermore, the small proportion of acoustic to optical modes implies a significant contribution of optical modes to κ_L. The reduction in phonon lifetimes suggests an increase in heat transport due to greater phonon scattering, which is evident from our experimental results, showing higher phonon–phonon scattering at elevated temperatures. These results also indicate that at lower temperatures, the phonon–phonon scattering rate is significantly reduced compared to higher temperatures. This phenomenon is further related to the interplay between phonon–phonon and electron-phonon scattering, affecting coherence length in systems with disorder and strong spin-orbit coupling that exhibit the WAL effect. The observed linewidth in two phonon modes (^2A_g and ^3A_g) illustrates the presence of electron-phonon coupling in $HfAs_2$, as evidenced by the Raman results. These modes reveal that the system exhibits both electron-phonon and phonon–phonon interactions. This dual interaction is consistent with the trends observed in previous studies.[34,66] In addition, the heavy atoms with large spin-orbit coupling found in many topological materials also lead to a reduction in the bandwidth of the acoustic phonons, limiting the available phase space for phonon–phonon scattering, as discussed above.

Understanding the underlying mechanisms can provide insights into enhancing the thermoelectric performance of topological semimetals. This includes strategies such as increasing the density of states near the Fermi level, optimizing carrier concentration, and reducing lattice thermal conductivity. Notable examples include $NbAs_2$, which exhibits a high transverse power factor of 850 $\mu W\,cm^{-1}\,K^{-2}$, and Cd_2As_3, showing a ZT of 1.1 under an applied magnetic field,[67,68] making them promising candidates for high thermoelectric performance. Poudel et al. (2008) demonstrated that creating nanostructures within the bulk of Bi_2Te_3 significantly enhances phonon scattering, leading to reduced thermal conductivity. This enhanced phonon scattering mechanism does not compromise electrical conductivity, resulting in a high ZT value.[69] Similarly, TaP has been identified for its non-saturating quantized thermoelectric Hall conductivity and thermopower, making it an excellent semimetal candidate for thermoelectric applications below room temperature.[70] Our findings contribute to the understanding and potential utilization of these new topological materials for energy harvesting applications.

3. Conclusion

It is summarized that the single crystals of $HfAs_2$ were grown by using the CVT method and simultaneously studied their

electronic and phonon properties using transport, ARPES, and Raman spectroscopy. The Fermi surface and electronic band structure were studied by ARPES and DFT calculations revealed that the nontrivial topological surface states show that $HfAs_2$ is a topological nodal semimetal. The transport properties of $HfAs_2$ demonstrate the higher electronic carrier density and carrier mobility, which are correlated with electron-hole compensation and topological states. The magnetoresistance measurement further revealed the weak antilocalization at low temperatures associated with the disorder and/or spin-orbit coupling, which was further validated by Raman and phonon calculations, which contributes to both electron and phonon scattering. The Raman measurement revealed the anharmonic phonon–phonon and electron-phonon interactions supported by the low lattice thermal conductivity and phonon lifetime. These results can further provide a route toward the thermoelectric properties of the new materials, especially topological materials.

4. Experimental Section

Transport Measurements: Electrical transport measurements were performed with the four-probe technique on the rectangular crystal with a 9 T magnetic field applied measured by using a 16 T PPMS (Quantum Design, Inc.) at the Steady High Magnetic Field Facilities, High Magnetic Field Laboratory, (HMFL), CAS, Hefei, China. The low-field resistivity and MR were measured with a standard four-probe punk using a 14 T PPMS (Quantum Design, Inc.). Gold wires were used to make electrodes on the bulk $HfAs_2$ sample with silver epoxy to make four contacts.

ARPES Measurements: ARPES experiments were performed with a Scienta DA30L electron spectrometer at the beamline 13U of the National Synchrotron Radiation Laboratory (NSRL), Hefei. Horizontal polarization of incident light ($h\nu$ = 30 to 45 eV) was used to investigate the electronic structures of $HfAs_2$. The angular resolution was 0.3° and the combined instrumental energy resolution was better than 18 meV. All samples were cleaved in situ at 12 K and measured under a vacuum better than 8×10^{-11} mbar.

Raman Measurements: The Raman scattering (RS) spectra were measured under excitation from a single-frequency diode laser λ = 515 nm (2.41 eV). The excitation light was focused using a 50 × long-working distance objective with a 0.55 numerical aperture (NA) producing a spot of ≈1 µm diameter. The signal was collected via the same microscope objective (the backscattering geometry), sent through a 0.75 m monochromator, and then detected by using a liquid nitrogen-cooled charge-coupled device (CCD) camera. The polarization-resolved RS measurements were performed in two co-(XX) and cross-linear-(XY) configurations, which correspond to the parallel and perpendicular orientation of the excitation and detection polarization axes, respectively. The analysis of the RS signal was done using a motorized half-wave plate, mounted on top of the microscope objective, which provides simultaneous rotation of polarization axis in the XX and XY configurations.

Calculation Details: The electronic structure calculations were carried out with the projector-augmented wave approach within the density functional theory framework, utilizing the VASP package.[71] A plane-wave energy cut-off of 650 eV was employed in the study. The generalised gradient approximation (GGA) method was utilized as the exchange-correlation function.[72] The calculations of electronic structures were performed with a 6 × 12 × 4 Monkhorst-Pack k-mesh, incorporating the spin-orbit coupling self-consistently. The VASPWANNIER90 interface was employed in the study, utilizing s and d orbitals of Hf atoms, as well as p orbitals of As atoms, to generate a tight-binding Hamiltonian without performing the procedure for maximizing localization.[73,74] The calculation of the surface state was performed using the semi-infinite Green's function approach incorporated in the Wanniertools.[75,76]

For the lattice-dynamics calculation, the phonon dispersions and the density of states (DOS) were attained from the finite displacement method employing the Phonopy package[77,78] with VASP as a force calculator. These calculations were done together with third-order force constants calculations to compute the phonon lifetimes using single-mode relaxation time approximation (SM-RTA) via the Phono3py package.[64] The SM-RTA offers a solution to the linearised phonon Boltzmann transport equation that relates the lattice thermal conductivity to contributions arising from individual phonon modes. To calculate the second-and third-order inter-atomic force constants, the same 2 × 3 × 2 supercell was used with 4 × 6 × 3 and 2 × 3 × 2 Monkhorst–Pack k-mesh, respectively.[79,80] This was sufficient for the convergence of the phonon dispersion. For evaluating the third-order inter-atomic force constants, pairwise atomic displacements are required. The 300 eV kinetic-energy cutoff for carrying out the geometry optimization is employed for force calculations. However, the explicit treatment of spin-orbit coupling is not included as the phonon frequencies in the electronic-structure calculations are unlikely to be affected, but it considerably raises the computational cost.[81]

Supporting Information

Supporting Information is available from the Wiley Online Library or from the author.

Acknowledgements

This research was supported by the National Natural Science Foundation of China (Grants No. 62150410438), and the Beihang Hefei Innovation Research Institute (project no. BHKX-19-02). R.I. and F.X acknowledge the support by the National Science Foundation under Grant No.OIA-2229498 and acknowledge the access to the computing facility Cheaha at the University of Alabama at Birmingham. The authors acknowledge support from the National Science Centre, Poland, through Grants No. 2018/31/B/ST3/02111 (N.Z. and M.R.M.) and No. 2017/27/B/ST3/00205 (A.B.). The work at Princeton University is supported by the US Department of Energy, Office of Science (grant no BOE/BES DE-FG-02-05ER46200), National Quantum Information Science Research Centers, Quantum Science Center (at ORNL), Gordon and Betty Moore Foundation (GBMF9461), and Princeton University. The authors also acknowledge beamline 13U of the National Synchrotron Radiation Laboratory (NSRL) for the ARPES experiments and High Magnetic Field Laboratory, Hefei Institutes of Physical Science, Chinese Academy of Sciences for transport measurement.

Conflict of Interest

The authors declare no conflict of interest.

Data Availability Statement

The data that support the findings of this study are available from the corresponding author upon reasonable request.

Keywords

electronic structures, phonon dynamics, thermal properties, topological semimetals, weak antilocalization

Received: December 28, 2023
Revised: May 28, 2024
Published online: June 26, 2024

[1] C. Shekhar, A. K. Nayak, Y. Sun, M. Schmidt, M. Nicklas, I. Leermakers, U. Zeitler, Y. Skourski, J. Wosnitza, Z. Liu, Y. Chen, W.

Schnelle, H. Borrmann, Y. Grin, C. Felser, B. Yan, *Nat. Phys.* **2105**, *11*, 645.
[2] Y. Y. Wang, Q. H. Yu, P. J. Guo, K. Liu, T. L. Xia, *Phys. Rev. B* **2016**, *94*, 041103.
[3] Z. Yuan, H. Lu, Y. Liu, J. Wang, S. Jia, *Phys. Rev. B* **2016**, *93*, 184405.
[4] M. N. Ali, J. Xiong, S. Flynn, J. Tao, Q. D. Gibson, L. M. Schoop, T. Liang, N. Haldolaarachchige, M. Hirschberger, N. P. Ong, R. J. Cava, *Nature* **2014**, *514*, 205.
[5] C. Herring, *Phys. Rev.* **1937**, *52*, 365.
[6] N. P. Armitage, E. J. Mele, A. Vishwanath, *Rev. Mod. Phys.* **2018**, *90*, 015001.
[7] A. Burkov, *Annual Rev. Cond. Matt. Phys.* **2018**, *9*, 359.
[8] X. Huang, L. Zhao, Y. Long, P. Wang, D. Chen, Z. Yang, H. Liang, M. Xue, H. Weng, Z. Fang, X. Dai, *Phys. Rev. X* **2015**, *5*, 031023.
[9] C. Zhang, C. Guo, H. Lu, X. Zhang, Z. Yuan, Z. Lin, J. Wang, S. Jia, *Phys. Rev. B* **2015**, *92*, 041203.
[10] H. Z. Lu, S. Q. Shen, *Phys. Rev. B* **2015**, *92*, 035203.
[11] B. Yan, F. Claudia, *Annu. Rev. of Cond. Matt. Phys.* **2017**, *8*, 337.
[12] A. A. Soluyanov, D. Gresch, Z. Wang, Q. Wu, M. Troyer, X. Dai, B. A. Bernevig, *Nature* **2015**, *527*, 495.
[13] G. Autes, D. Gresch, M. Troyer, A. A. Soluyanov, O. V. Yazyev, *Phys. Rev. Lett.* **2016**, *117*, 066402.
[14] B. Q. Lv, T. Qian, H. Ding, *Rev. Mod. Phys.* **2021**, *93*, 025002.
[15] M. Z. Hasan, G. Chang, I. Belopolski, G. Bian, S. Y. Xu, J. X. Yin, *Nat. Rev. Mater.* **2021**, *6*, 784.
[16] Z. S. Shao, Y. Wang, C. Xu, R. Sankar, A. J. Breindel, C. Cao, M. M. Fogler, A. J. Millis, F. Chou, Z. Li, T. Timusk, M. B. Maple, D. N. Basov, *Proc. Natl. Acad. Sci. U. S. A.* **2019**, *116*, 1168.
[17] C. Sims, M. M. Hosen, H. Aramberri, C. Y. Huang, G. Dhakal, K. Dimitri, F. Kabir, S. Regmi, X. Zhou, T. R. Chang, H. Lin, *Phys. Rev. Mater.* **2020**, *4*, 054201.
[18] X. Zhou, C. H. Hsu, H. Aramberri, M. Iraola, C. Y. Huang, J. L. Mañes, M. G. Vergniory, H. Lin, N. Kioussis, *Phys. Rev. B* **2021**, *104*, 125135.
[19] J. Bannies, E. Razzoli, M. Michiardi, H. H. Kung, I. S. Elfimov, M. Yao, A. Fedorov, J. Fink, C. Jozwiak, A. Bostwick, E. Rotenberg, *Phys. Rev. B* **2021**, *103*, 155144.
[20] L. Aggarwal, S. Gayen, S. Das, R. Kumar, V. Süß, C. Felser, C. Shekhar, G. Sheet, *Nat. Commun.* **2017**, *8*, 1.
[21] M. D. Zhang, X. Y. Hou, Q. Wang, Y. Y. Wang, L. X. Zhao, Z. Wang, Y. D. Gu, F. Zhang, T. L. Xia, Z. A. Ren, G. F. Chen, *Phys. Rev. B* **2020**, *102*, 085139.
[22] F. Han, N. Andrejevic, T. Nguyen, V. Kozii, Q. T. Nguyen, T. Hogan, Z. Ding, R. Pablo-Pedro, S. Parjan, B. Skinner, A. Alatas, *Nat. Commun.* **2020**, *11*, 1.
[23] R. Lundgren, P. Laurell, G. A. Fiete, *Phys. Rev. B* **2014**, *90*, 165115.
[24] C. H. A. N. Ching-Kit, N. Lindner, G. Refael, M. A. Qiong, S. Xu, N. Gedik, *U.S. Patent* **2018**, *10 090*, 466.
[25] G. Dhakal, M. M. Hosen, W. C. Chiu, B. Singh, C. Y. Huang, K. Dimitri, B. Wang, F. Kabir, C. Sims, S. Regmi, W. Neff, *Phys. Rev. Res.* **2021**, *3*, 023170.
[26] N. Kumar, Y. Sun, N. Xu, K. Manna, M. Yao, V. Süss, I. Leermakers, O. Young, T. Förster, M. Schmidt, H. Borrmann, *Nat. Commun.* **2017**, *8*, 1.
[27] J. Du, Z. Lou, S. Zhang, Y. Zhou, B. Xu, Q. Chen, Y. Tang, S. Chen, H. Chen, Q. Zhu, H. Wang, *Phys. Rev. B* **2018**, *97*, 245101.
[28] V. M. Plisson, X. Yao, Y. Wang, G. Varnavides, A. Suslov, D. Graf, E. S. Choi, H. Y. Yang, Y. Wang, M. Romanelli, G. McNamara, *Adv. Mater.* **2024**, *36*, 2310944.
[29] H. Y. Yang, X. Yao, V. Plisson, S. Mozaffari, J. P. Scheifers, A. F. Savvidou, E. S. Choi, G. T. McCandless, M. F. Padlewski, C. Putzke, P. J. Moll, *Nat. Commun.* **2021**, *12*, 5292.
[30] J. Coulter, R. Sundararaman, P. Narang, *Phys. Rev. B* **2018**, *98*, 115130(R).
[31] F. Jin, X. Ma, P. Guo, C. Yi, L. Wang, Y. Wang, Q. Yu, J. Sheng, A. Zhang, J. Ji, Y. Tian, *Phys. Rev. B* **2016**, *94*, 094302.
[32] Y. Wu, B. Hou, Y. Chen, J. Cao, H. Shao, Y. Zhang, C. Ma, H. Zhu, R. Zhang, H. Zhang, *npj Comput. Mater.* **2021**, *7*, 145.
[33] G. Varnavides, A. S. Jermyn, P. Anikeeva, C. Felser, P. Narang, *Nat. Commun.* **2020**, *11*, 4710.
[34] J. Coulter, G. B. Osterhoudt, C. A. C. Garcia, Y. Wang, V. M. Plisson, B. Shen, N. Ni, K. S. Burch, P. Narang, *Phys. Rev. B* **2019**, *100*, 220301(R).
[35] B. Xu, Y. M. Dai, L. X. Zhao, K. Wang, R. Yang, W. Zhang, J. Y. Liu, H. Xiao, G. F. Chen, S. A. Trugman, J.-X. Zhu, A. J. Taylor, D. A. Yarotski, R. P. Prasankumar, X. G. Qiu, *Nat. Commun.* **2017**, *8*, 14933.
[36] A. Sharafeev, V. Gnezdilov, R. Sankar, F. C. Chou, P. Lemmens, *Phys. Rev. B* **2017**, *95*, 235148.
[37] M. Holland, *Phys. Rev.* **1932**, *132*, 2461.
[38] J. Callaway, *Phys. Rev.* **1959**, *113*, 1046.
[39] Z. Tian, J. Garg, K. Esfarjani, T. Shiga, J. Shiomi, G. Chen, *Phys. Rev. B* **2012**, *85*, 184303.
[40] W. Li, J. Carrete, G. K. H. Madsen, N. Mingo, *Phys. Rev. B* **2016**, *93*, 205203.
[41] C. Rincon, F. Ramirez, *J. Appl. Phys.* **1992**, *72*, 4321.
[42] G. B. Osterhoudt, Y. Wang, C. A. C. Garcia, V. M. Plisson, J. Gooth, C. Felser, P. Narang, K. S. Burch, *Phys. Rev. X* **2021**, *11*, 011017.
[43] Z. Muhammad, F. Wali, G. Hussain, R. Islam, S. Ullah, P. Wu, F. Khan, C. Autieri, Y. Zhang, T. Alshahrani, W. Zhao, *J. Mater. Chem. C* **2023**, *11*, 2608.
[44] A. M. Lindenberg, I. Kang, S. L. Johnson, T. Missalla, P. A. Heimann, Z. Chang, J. Larsson, P. H. Bucksbaum, H. C. Kapteyn, H. A. Padmore, R. W. Lee, J. S. Wark, R. W. Falcone, *Phys. Rev. Lett.* **2000**, *84*, 111.
[45] S. Rundqvist, B. Carlsson, *Acta Chem. Scand.* **1968**, *22*, 2395.
[46] J. Wang, L. Li, W. You, T. Wang, C. Cao, J. Dai, Y. Li, *Sci. Rep.* **2017**, *7*, 1.
[47] M. N. Ali, J. Xiong, S. Flynn, J. Tao, Q. D. Gibson, L. M. Schoop, T. Liang, N. Haldolaarachchige, M. Hirschberger, N. P. Ong, R. J. Cava, *Nature* **2014**, *514*, 205.
[48] T. Liang, Q. Gibson, M. N. Ali, M. Liu, R. J. Cava, N. P. Ong, *Nat. Mater.* **2014**, *14*, 280.
[49] K. Wang, D. Graf, L. Li, L. Wang, C. Petrovic, *Sci. Rep.* **2014**, *14*, 280.
[50] T. Kawamura, S. D. Sarma, *Phys. Rev. B* **1992**, *45*, 3612.
[51] S. Gautam, V. Aggarwal, B. Singh, V. P. S. Awana, R. Ganesan, S. S. Kushvaha, *Sci. Rep.* **2022**, *12*, 1.
[52] H.-J. Kim, K.-S. Kim, J.-F. Wang, M. Sasaki, N. Satoh, A. Ohnishi, M. Kitaura, M. Yang, L. Li, *Phys. Rev. Lett.* **2013**, *111*, 246603.
[53] C. L. Zhang, S. Y. Xu, I. Belopolski, Z. Yuan, Z. Lin, B. Tong, G. Bian, N. Alidoust, C. C. Lee, S. M. Huang, T. R. Chang, *Nat. Commun.* **2016**, *7*, 1.
[54] F. C. Chen, Y. Fei, S. J. Li, Q. Wang, X. Luo, J. Yan, W. J. Lu, P. Tong, W. H. Song, X. B. Zhu, L. Zhang, *Phys. Rev. Lett.* **2020**, *124*, 236601.
[55] https://www.cryst.ehu.es/cgi-bin/cryst/programs/nph-polarizationselrules
[56] Y. Tian, S. Jia, R. J. Cava, R. Zhong, J. Schneeloch, G. Gu, K. S. Burch, *Phys. Rev. B* **2017**, *95*, 094104.
[57] M. Balkanski, R. F. Wallis, E. Haro, *Phys. Rev. B* **1983**, *28*, 1928.
[58] M. Balkanski, R. F. Wallis, E. Haro, *Phys. Rev. B* **1983**, *28*, 1928.
[59] A. M. Hofmeister, *Proc. Nat. Acad. Sci. U. S. A.* **2007**, *104*, 9192.
[60] W. Rahim, J. M. Skelton, D. O. Scanlon, *J. Mater. Chem. A* **2020**, *8*, 16405.
[61] J. Carrete, N. Mingo, S. Curtarolo, *Appl. Phys. Lett.* **2014**, *105*, 101907.
[62] L. Bergman, D. Alexson, P. L. Murphy, R. J. Nemanich, M. Dutta, M. A. Stroscio, C. Balkas, H. Shin, R. F. Davis, *Phys. Rev. B* **2014**, *59*, 1999.
[63] L. D. Whalley, J. M. Skelton, J. M. Frost, A. Walsh, *Phys. Rev. B* **2016**, *94*, 220301.
[64] A. Togo, L. Chaput, I. Tanaka, *Phys. Rev. B* **2015**, *91*, 094306.
[65] R. Cuscó, E. Alarcón-Lladó, J. Ibáñez, L. Artús, J. Jiménez, B. Wang, M. J. Callahan, *Phys. Rev. B* **2007**, *75*, 165202.

[66] Y. S. Ponosov, S. V. Streltsov, *Phys. Rev. B* **2017**, *96*, 214503.
[67] S. Wu, X. Wang, X. Mi, S. Zheng, K. Yang, Z. Zhou, H. Wang, G. Han, X. Lu, Y. Pan, G. Wang, *Adv. Energy Mater.* **2024**, 2400184.
[68] H. Wang, X. Luo, W. Chen, N. Wang, B. Lei, F. Meng, C. Shang, L. Ma, T. Wu, X. Dai, Z. Wang, *Sci. Bull.* **2018**, *63*, 411.
[69] B. Poudel, Q. Hao, Y. Ma, Y. Lan, A. Minnich, B. Yu, X. Yan, D. Wang, A. Muto, D. Vashaee, X. Chen, *Science* **2008**, *320*, 634.
[70] F. Han, N. Andrejevic, T. Nguyen, V. Kozii, Q. T. Nguyen, T. Hogan, Z. Ding, R. Pablo-Pedro, S. Parjan, B. Skinner, A. Alatas, *Nat. Commun.* **2020**, *11*, 6167.
[71] G. Kresse, J. Furthmüller, *Phys. Rev. B* **1996**, *54*, 11169.
[72] J. P. Perdew, K. Burke, M. Ernzerhof, *Phys. Rev. Lett.* **1996**, *77*, 3865.
[73] A. A. Mostofi, J. R. Yates, Y.-S. Lee, I. Souza, D. Vanderbilt, N. Marzari, *Comp. Phys. Commun.* **2008**, *178*, 685.
[74] N. Marzari, D. Vanderbilt, *Phys. Rev. B* **1997**, *56*, 12847.
[75] Q. Wu, S. Zhang, H.-F. Song, M. Troyer, A. A. Soluyanov, *Comp. Phys. Commun.* **2018**, *224*, 405.
[76] M. P. L. Sancho, J. M. L. Sancho, J. M. L. Sancho, J. Rubio, *J. Phys. F:Met. Phys.* **1985**, *15*, 851.
[77] A. Togo, F. Oba, I. Tanaka, *Phys. Rev. B* **2008**, *78*, 134106.
[78] A. Togo, I. Tanaka, *Scr. Mater.* **2015**, *108*, 1.
[79] K. Parlinski, Z. Li, Y. Kawazoe, *Phys. Rev. Lett.* **1997**, *78*, 4063.
[80] G. Kresse, J. Furthmüller, J. Hafner, *Europhys. Lett.* **1995**, *32*, 729.
[81] A. Romero, M. Cardona, R. K. Kremer, R. Lauck, G. Siegle, J. Serrano, X. C. Gonze, *Phys. Rev. B* **2008**, *78*, 224302.